Supplementary information for 'Quantum delayed-choice experiment with a beam splitter in a quantum superposition'

Shi-Biao Zheng[1],* You-Peng Zhong[2], Kai Xu[2], Qi-Jue Wang[2], H. Wang[2], Li-Tuo Shen[1], Chui-Ping Yang[3], John M. Martinis[4],† A. N. Cleland[5],‡ and Si-Yuan Han[6,7]

[1]*Department of Physics, Fuzhou University, Fuzhou 350116, China*
[2]*Department of Physics, Zhejiang University, Hangzhou 310027, China*
[3]*Department of Physics, Hangzhou Normal University, Hangzhou 310036, China*
[4]*Department of Physics, University of California, Santa Barbara, California 93106, USA*
[4]*Institute for Molecular Engineering, University of Chicago, Chicago, Illinois 60637, USA*
[6]*Department of Physics and Astronomy, University of Kansas, Lawrence, Kansas 66045, USA*
[7]*Beijing National Laboratory for Condensed Matter Physics, Institute of Physics, Chinese Academy of Sciences, Beijing 100190, China*

QUANTUM CIRCUIT AND QUBIT-RESONATOR INTERACTION CONTROL

The quantum circuit used to implement our quantum delayed-choice experiment consists of two phase qubits coupled to a superconducting coplanar waveguide resonator, as shown in Fig. S.1. The sample, as described in Ref. 1, involves four qubits, two of which are not used in our experiment and not shown in the circuit diagram. The resonator has a fixed frequency of 6.205 GHz, while the frequency of each qubit is tunable through a flux bias coil. Neglecting the effects of higher levels of the qubits, the qubit-resonator interaction Hamiltonian in the interaction picture is given by

$$H=\hbar\sum_{j=1}^{2}\Omega_j\left(e^{i\Delta_j t}\sigma_j^{+}a+e^{-i\Delta_j t}\sigma_j^{-}a^{\dagger}\right), \tag{S1}$$

where σ_j^{+} and σ_j^{-} are the raising and lowering operators for qubit j, a and $a^{\dagger}$ the annihilation and creation operators of the field in the resonator, and Ω_j is the coupling strength between qubit j and the resonator with the detuning Δ_j. The Hamiltonian describes the coherent energy exchange between the qubits and the resonator. When $\Delta_j\gg\Omega_j$ the photon transfer probability between qubit j with the resonator is negligible, implying their interaction is effectively switched off. On the other hand, when $\Delta_j=0$ and $\Delta_k\gg\Omega_k$ $(j,k=1,2$ and $j\neq k)$ the interaction between qubit j and the resonator is described by the Jaynes-Cummings Hamiltonian. The qubit frequency tunability allows us to freely control the qubit-resonator interaction.

THE FIRST RAMSEY PULSE WITH A COHERENT FIELD IN THE RESONATOR

The coherent field state $|\alpha\rangle$ stored in the resonator can be expressed as a superposition of photon number states: $|\alpha\rangle=\sum_{n=0}^{\infty}C_n|n\rangle$, where $C_n=\exp\left(-|\alpha|^2/2\right)\alpha^n/\sqrt{n!}$ is the probability amplitude for having n photons. The Rabi oscillation frequency associated with the photon-number state $|n\rangle$ is $\sqrt{n}\Omega$. After an interaction time $t_\alpha=\pi/(4|\alpha|\Omega)$ the state of the qubit-resonator system evolves to

$$|\Psi\rangle=\sum_{n=0}^{\infty}\left[C_n\cos(\sqrt{n}\Omega t_\alpha)|g\rangle-iC_{n+1}\sin(\sqrt{n+1}\Omega t_\alpha)|e\rangle\right]|n\rangle. \tag{S2}$$

The coherent field has a Poissonian photon-number distribution, with the mean photon number $\bar{n}=|\alpha|^2$ and variance $\Delta n=|\alpha|$. When the field amplitude is large, Δn is much smaller than $\bar{n}$. In this case, we have $C_{n+1}/C_n=\alpha/\sqrt{n+1}\simeq e^{i\vartheta}$ and $\sqrt{n}\Omega t_\alpha\simeq|\alpha|\Omega t_\alpha=\pi/4$, where ϑ is the argument of the complex amplitude α. For $\vartheta=0$, the total state $|\Psi\rangle$ is approximately a product of the qubit state $(|g\rangle-i|e\rangle)/\sqrt{2}$ with the field state $|\alpha\rangle$.

EXPERIMENTAL SEQUENCE FOR RAMSEY INTERFERENCE

The state $|\psi_{b,i}\rangle$ of Eq. (3) of the main text with $\varphi\neq0,\pi/2$ is generated by coherently pumping photons into the resonator one by one through the ancilla qubit, emploiting an algorithm theoretically proposed in Ref. 2. Experimental

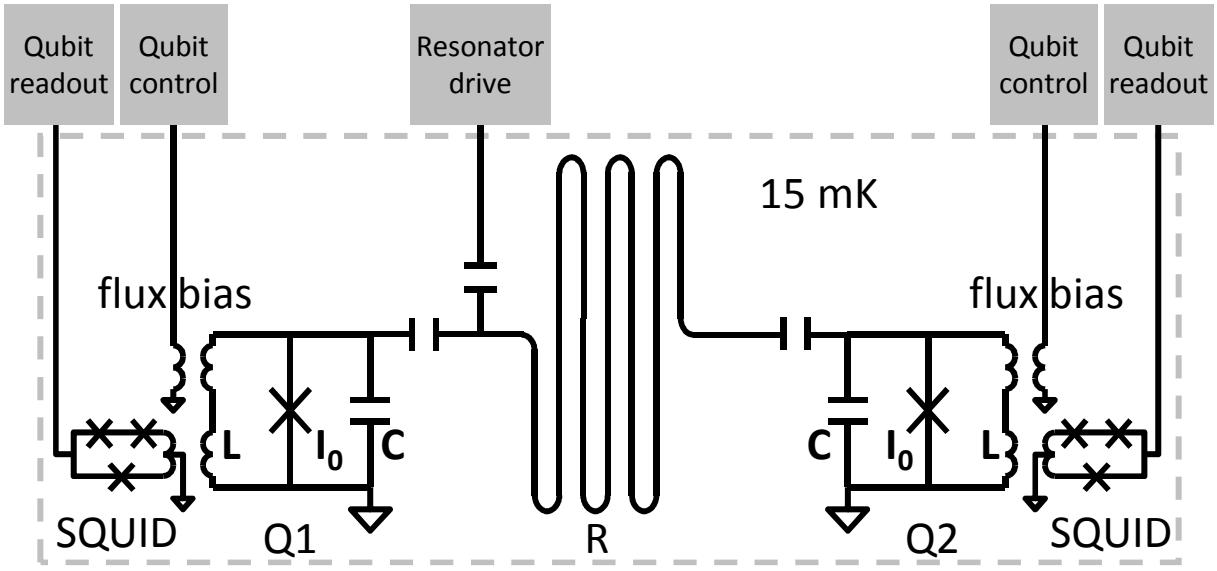

Figure S1: (Color online) Circuit schematic. Two phase qubits are coupled to a superconducting coplanar waveguide resonator via capacitors. The detuning between each qubit and the resonator is adjusted through a flux bias coil, enabling the relevant qubit-resonator interaction to be effectively switched on and off. External microwave pulses are coupled to the qubits through the flux bias coil, and to the resonator through the capacitor on the left side of the resonator. The coupling strengths of the resonator to the two qubits are $2\pi \times 17.5$ MHz and $2\pi \times 17.7$ MHz, respectively. The energy relaxation times for these two qubits are 520 ns and 560 ns, respectively, and the Ramsey dephasing times for both qubits are about 150 ns. The energy relaxation time of the resonator is 3.0 μs without measurable dephasing.

implementation of this algorithm in a superconducting resonator involves alternative, well-controlled qubit drive operations and qubit-resonator swap operations, as detailedly described in Refs. 3 and 4 and illustrated in Fig. S2. Here the qubit drive operation is achieved by applying a resonant microwave pulse through the flux bias coil. To decrease the reasonable cutoff in the Fock-state expansion, we first generate the supersotion state $\mathcal{N}(\cos\varphi\,|\alpha/2\rangle - \sin\varphi\,|-\alpha/2\rangle)$ with $\alpha = 2$ (the cutoff is $n = 4$), and then displace it in phase space by an amount $\alpha/2$, achieving the state $|\psi_{b,i}\rangle$. The displacement operation is performed using a microwave pulse capacitively coupled to the resonator. For $\varphi = 0$, we directly generate $|\psi_{b,i}\rangle$ from the vacuum state by performing the displacement operation $D(\alpha)$. We produce the states $|\psi_{b,i}\rangle$ for $\varphi = 0$, $\pi/8$, $\pi/4$, $3\pi/8$, $\pi/2$, with the fidelities being 0.898 ± 0.023, 0.702 ± 0.021, 0.726 ± 0.028, 0.760 ± 0.017, and 0.992 ± 0.004, respectively.

After preparation of $|\psi_{b,i}\rangle$, we achieve the first pulse R_1 by turning on the interaction between the test qubit and the resonator for a time t_α. For the observation of the Ramsey signal displayed in Fig. 2a of the main text, R_1 is directly followed by a phase-tunable, on-resonance microwave$\pi/2$ pulse $R_2(\theta)$ applied to the qubit. For different φ, the Ramsey interference pattern is constructed by measuring the resulting excited-state probability of the test qubit as a function of θ. To obtain the result shown in Fig. 2b of the main text, after R_1 an aditional iSwap gate is applied to the resonator field and the ancilla, as shown in Fig. S.2. The wave and particle behaviors of the test qubit is post-selected by detecting the state of the ancilla.

MEASUREMENT OF WIGNER FUNCTIONS

To reconstruct the WF of the reduced density operator of the resonator field without reading-out the state of the test qubit, we perform the displacement operation $D(-\chi)$ after the second Ramsey pulse, and then let the ancilla qubit initially in the ground state interact with the resonator field for a variable time τ, followed by the measurement of the state of the ancilla. The measured probability $P_e(\tau)$ for the ancilla being in the excited state, as a function of τ, is used to infer the diagonal elements of the displaced density matrix of the resonator field and hence the value of the WF at point χ in phase space [3, 4].

To map out the WF of the resonator field associated with the states $|g\rangle$ and $|e\rangle$ of the test qubit, we perform the joint qubit-resonator tomography, which requires reading-out both the test and ancilla qubits simultaneously, as described in Ref. 5.

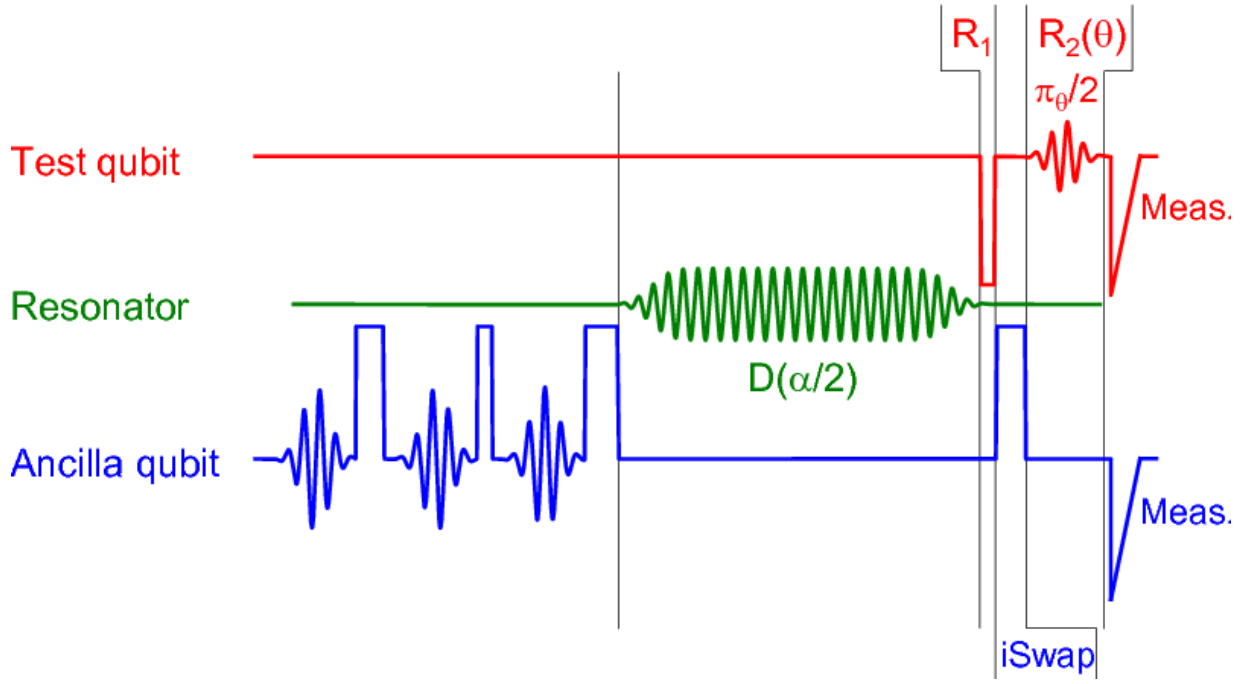

Figure S2: (Color online) Experimental sequence for Ramsey interference. Three microwave pulses (blue sinusoids) and three qubit-resonator swap pulses (blue squares) applied alternately, are used to generate the superposition state $\mathcal{N}(\cos\varphi\,|\alpha\rangle - \sin\varphi\,|0\rangle)$ with $\alpha = 2$ (the cutoff is $n = 4$) in the resonator. The ancilla qubit returns to its ground state and no further operation is performed on it for measurement of the Ramsey signal of Fig. 2a of the main text. The displacement pulse $\mathrm{D}(\alpha/2)$ further turns the resonator field state into $|\psi_{b,i}\rangle$ (see Eq. (3) of the main text). R_1 on the test qubit is implemented by turning on the qubit-resonator interaction for a time t_α (red square), while $\mathrm{R}_2(\theta)$ achieved by applying a phase-tunable, on-resonance microwave pulse to the test qubit (red sinusoid). For different φ, the resulting excited-state probability of the test qubit as a function of θ is measured (red triangle pulse), which forms the Ramsey interference pattern, as shown in Fig. 2a of the main text. To distinguish between the wave and particle outcomes as shown in Fig. 2b of the main text, after R_1 the state of the resonator is examined by the ancilla qubit using an iSwap gate (the fourth blue square), followed by ancilla state detection (the blue triangle pulse).

In Fig. S3, we present the measured WFs of the field state in the resonator for $\varphi = \pi/8,\, 3\pi/8$. Panel a (d) shows the WFs when the qubit state is traced out, while b (e) and c (f) exhibit the WFs associated with the outcomes $|g\rangle$ and $|e\rangle$ for $\varphi = \pi/8$ $(3\pi/8)$, respectively. In each panel, the simulated and measured WFs are shown in the upper and lower rows, respectively. Experimental imperfections are not included in numerical simulation. As expected, due to the quantum coherence between the present and absent states of the QBS the WF for each case exhibits a nonclassical feature around $\chi = 1$. When the qubit state is measured, the quantum interference and hence the negativity of the WF are enhanced. These results, together with those shown in Fig. 2 of the main text, reveal the quantum nature of the QBS for a wide range of the parameter φ.

OBSERVING TRANSITION FROM QUANTUM TO CLASSICAL BEAM SPLITTER

Another benefit of this experimental implementation is that it allows the observation of the transition from a quantum to a classical beam splitter. To demonstrate this, we now delay the interaction between the test qubit and the resonator for a time T after the QBS has been prepared in the cat state $|\psi_{b,i}\rangle$. Then, just before the test qubit-resonator interaction, the field density operator is given by [6]

$$\begin{aligned}\rho_b \;=\; & \mathcal{N}^2[\cos^2\varphi|\alpha'\rangle\langle\alpha'| + \sin^2\varphi|0\rangle\langle 0| \\ & -\frac{1}{2}e^{-|\alpha|^2(1-e^{-\gamma T})/2}\sin(2\varphi)(|\alpha'\rangle\langle 0| + |0\rangle\langle\alpha'|)], \qquad (S3)\end{aligned}$$

where $\alpha' = \alpha e^{-\gamma T/2}$ and γ is the decay rate of a photon in the resonator; we have ignored imperfections in the cat state preparation. In our experimental setup the single-photon lifetime is $\tau = 1/\gamma \simeq 3.0\ \mu$s. The qubit-resonator

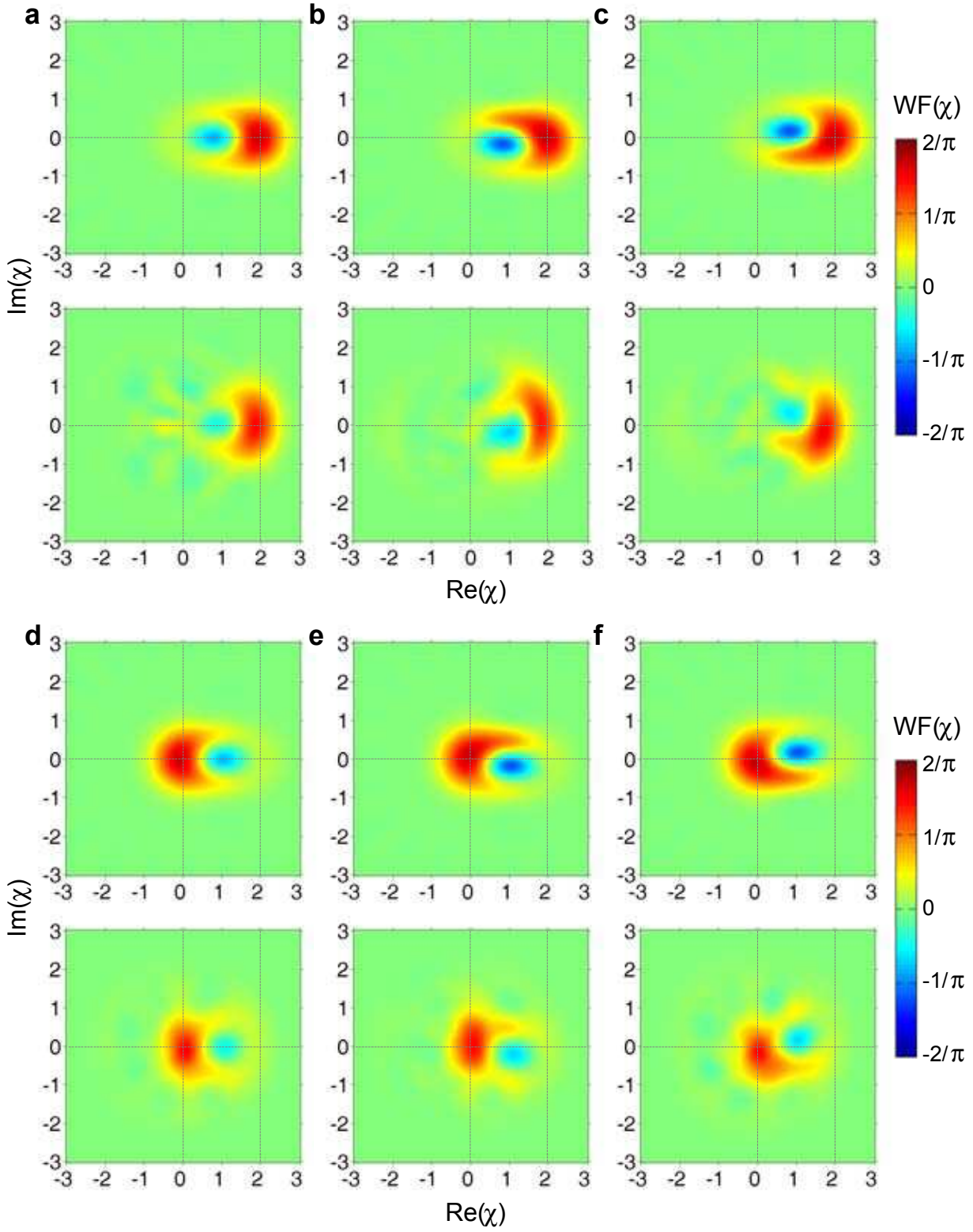

Figure S3: (Color online) Wigner tomography of the quantum beam splitter state. Panels a to c (d to f) display the WFs for $\varphi = \pi/8$ ($3\pi/8$). The parameters α and θ are as in Fig. 3 of the main text. Shown here are the reconstructed WFs of the resonator field for the three cases from left to right: (a and d) The qubit state is not read-out; (b and e) The qubit is measured in $|g\rangle$; (c and f) The qubit is measured in $|e\rangle$. In each panel, the simulated and measured WFs are shown in the upper and lower rows, respectively. Experimental imperfections are not included in numerical simulation. The minimum values of the measured WFs for $\varphi = \pi/8$ are -0.138 ± 0.020, -0.227 ± 0.021, and -0.193 ± 0.024, while those for $\varphi = 3\pi/8$ are -0.152 ± 0.025, -0.218 ± 0.029, and -0.215 ± 0.031, respectively.

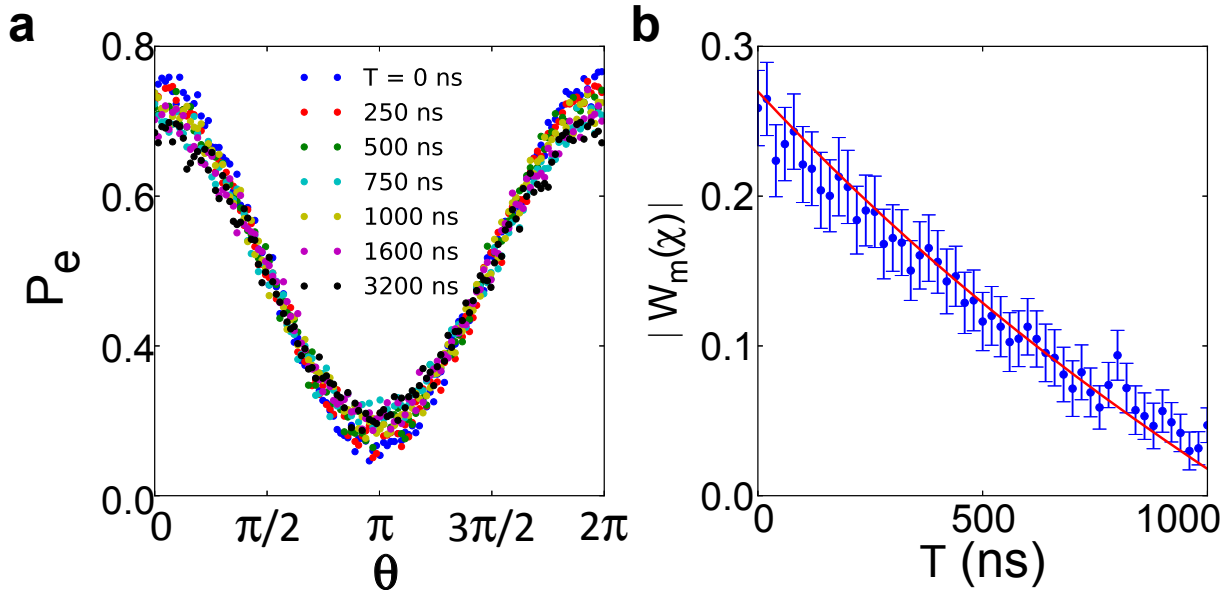

Figure S4: (Color online) Transition from a quantum to a classical beam splitter. (a) Measured Ramsey signals for different delays T, defined as the interval between the end of the cat state preparation and the start of the qubit-resonator interaction. The parameters are the same as those in Fig. S3. (b) Absolute value of the negative-valued minimum of the WF of the QBS state after R_2, without reading out the test qubit state, displayed versus T. The damping of the quantum coherence of the QBS is characterized by the decrease in the negativity of the WF. Error bars indicate the statistical variance. The line is a master-equation simulation taking the prepared cat state as the initial state for the decoherence evolution. The resonator single-photon lifetime is around 3.0 μs, with negligible pure dephasing.

interaction time is set to $t_{\alpha'} = \pi/(4\alpha'\Omega)$, so that after $R_2(\theta)$ the state component $|\alpha'\rangle|g\rangle$ approximately evolves to $|\alpha'\rangle|\psi_w\rangle$, while $|0\rangle|g\rangle$ evolves to $|0\rangle|\psi_p\rangle$.

In Fig. S4(a) we display the measured Ramsey interference signals for $\varphi = \pi/4$ with different delays T, showing that the fringe contrast is insensitive to the field decay, as expected. However, the quantum coherence between the active and inactive states of the QBS degrades much faster due to decoherence. Figure S4(b) shows the negative-valued minimum value of the WF as a function of delay T, with the WF measured after $R_2(\theta)$ but without reading out the test qubit state. The blue symbols are the measured results, whereas the red curve represents the simulated decay, taking the prepared cat state as the initial state. For $\gamma T = 1/3$, the amplitude of the coherent field is reduced by only 15%, but the absolute value of the minimum of the WF decays almost to zero, revealing the quick damping of the quantum coherence, which can be defined as the sum of the off-diagonal elements of the third term of Eq. (S3) in the photon-number representation [7]. Equation (S3) predicts that the quantum coherence is shrunk by a factor of about 0.51 after this delay. With a cat state of larger size and higher fidelity, as has been achieved in [3, 4, 8, 9], one could observe further decay of the quantum coherence of the QBS.

* Electronic address: t96034@fzu.edu.cn
† Electronic address: martinis@physics.ucsb.edu
‡ Electronic address: anc@uchicago.edu

[1] Y. P. Zhong *et al.*, *Nat. Commun* **5**, 3135 (2014).

[2] C. K. Law and J. H. Eberly, *Phys. Rev. Lett.* **76**, 1055 (1996).

[3] M. Hofheinz *et al.*, *Nature* **459**, 546 (2009).

[4] H. Wang *et al.*, *Phys. Rev. Lett.* **103**, 200404 (2009).

[5] X. Y. LinPeng *et al.*, *New J. Phys.* **15**, 125027 (2013).

[6] S. J. D. Phoenix, *Phys. Rev.* A **41**, 5132-5138 (1989).

[7] S. Deléglise *et al.*, *Nature* **455**, 510-514 (2008).

[8] G. Kirchmair *et al.*, *Nature* **495**, 205-209 (2013).

[9] B. Vlastakis *et al.*, *Science* **342**, 607 (2013).